Floris Andrea, Paderi Maurizio, Damiano Alfonso, Aymerich Francesco, Serpi Alessandro, "**Design criteria and methodology of a Multi-Rim Carbon-fibre Flywheel to be integrated within a Large-Airgap PMSM**", in 46th Annual Conference of the IEEE Industrial Electronics Society, IECON 2020, Volume 2020-October, Article number 9255025, pp. 913-919.

Design criteria and methodology of a Multi-Rim Carbon-fibre Flywheel to be integrated within a Large-Airgap PMSM

Andrea Floris(1), Maurizio Paderi(2), Alfonso Damiano(1), Francesco Aymerich(2), Alessandro Serpi(1)
(1)Department of Electrical and Electronic Engineering, (2)Department of Mechanical, Chemical and Material Engineering
University of Cagliari
Cagliari, Italy
andrea.floris86@unica.it

***Abstract*—The design of an Inner-Rotor Large-Airgap Permanent Magnet Synchronous Machine (IRLA-PMSM) is presented in this paper, whose distinctive feature consists of integrating a thick carbon-fibre cylindrical layer that acts as both a sleeve and a flywheel. This results in large airgap and makes simplified mechanical modelling generally used for sleeve design no more suitable. Therefore, an advanced mechanical modelling is presented in the paper, which is combined with an electromagnetic and energy modelling in order to make the analytical design procedure compliant with all the design targets and constraints. The proposed IRLA-PMSM is validated through finite element analyses, which regard both mechanical and electromagnetic aspects at different operating conditions.**

Keywords—Finite element analysis, Flywheels, Integrated design, Mechanical modelling, Permanent magnet machines

I. INTRODUCTION

Flywheel Energy Storage Systems (FESSs) represent a viable alternative to other ESSs in both vehicular and smart grid applications [1]–[3]. The most important strengths of FESS consist of high dynamic response, low maintenance, long lifecycle, high efficiency and low environmental impact. On the other hand, FESS design and manufacturing require advanced knowledge on different electromagnetic and mechanical aspects, which could increase costs and limit its applicability.

Several FESS topologies have been proposed in the literature, which can be roughly classified in split and integrated topologies [4], [5]. The latter consists of designing the flywheel as part of the rotor of the electrical machine, resulting in more compact and optimized configuration, but at the cost of a more complex design procedure and stricter constraints. Integrated topologies generally employ outer-rotor electrical machine configurations, mainly because the flywheel can span freely without affecting electromagnetic performance. However, inner-rotor configurations could be considered as well [6], [7]. For example, a Surface-Mounted Permanent Magnet Synchronous Machine (SPM) with an inner rotor structure could present smaller inner and outer rotor diameters compared to outer-rotor SPMs, thus guaranteeing the achievement of higher rotational speed. Furthermore, the outer stator acts as a preliminary enclosure, increasing the safety of the overall FESS. On the other hand, the flywheel acts as an additional air-gap in inner-rotor SPMs, increasing magnetic flux leakage and reducing torque density compared to outer-rotor SPMs.

In this context, the design of Inner-Rotor Large-Airgap Permanent Magnet Synchronous Machine (IRLA-PMSM) that integrates a carbon-fibre flywheel is presented in this paper. Differently from most of the configurations proposed in the literature, an inner rotor configuration has been selected, in which the rotor is surrounded by a thick carbon-fibre cylindric layer, which acts as both the flywheel and the sleeve, thus ensuring PM containment at any operating condition, as well as storing and delivering the required amount of energy. Such a large carbon-fibre layer requires the employment of advanced mechanical modelling, which has to be integrated within electromagnetic and energy modelling in order to define an enhanced analytical design procedure compared to that presented in previous works [8]–[10]. As a result, IRLA-PMSM design can be accomplished based on both design targets and constraints. The effectiveness of the proposed methodology has been verified through Finite Element Analyses (FEAs), which reveal the need for the advanced mechanical modelling considered in the paper, especially at high-speed operation.

II. IRLA-PMSM OVERVIEW

The overview of the proposed IRLA-PMSM is depicted in Fig. 1; this is designed for being competitive with electrochemical batteries for residential use, so it should be able to store 8 kWh of usable energy at 8 kW rated power. Additionally, its overall weight, radial and axial dimensions should not exceed 500 kg and 80 cm x 200 cm respectively, making it able to be transported and installed relatively easily.

The IRLA_PMSM rotor consists of several cylindric layers, among which the rotor yoke, the PM ring and the sleeve. The use of ferrite PMs have been preferred due to cost and availability issues of high-energy density PMs, by also reducing eddy current losses compared to NdFeB-based solutions. Regarding the sleeve, the choice falls on carbon-epoxy composite with unidirectional circumferential fibre distribution,

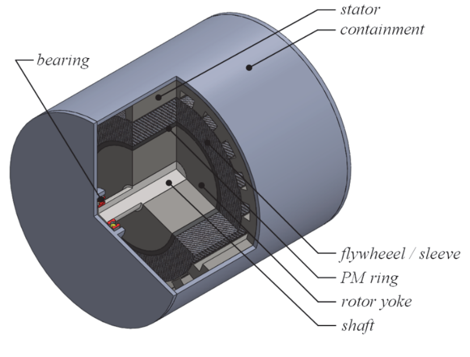

Fig. 1. IRLA-PMSM general overview.

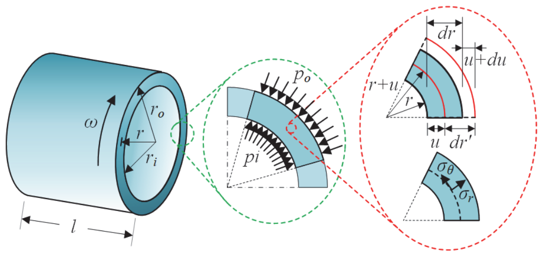

Fig. 2. Representation of a rotating cylinder and of its infinitesimal portion.

which maximizes the resistance and stiffness in circumferential direction, best fitting the typical stress distribution in rotating cylindrical components [11]. On the other hand, the epoxy matrix suffers from very low resistance in the radial direction, especially when it is subject to significant tensile stresses at high-speed operation. Consequently, the sleeve is prestressed through interference fit coupling [12], [13], not only to increase mechanical retention of PMs, but also to have a compression radial stress at zero speed, which reduces the maximum value of the tensile radial stress at maximum speed. Regarding the stator, a conventional three-phase winding is employed, while the material is a common silicon laminated steel, which guarantees very low specific losses at different frequencies of the magnetic flux density.

III. ANALYTICAL MECHANICAL MODELLING

In order to investigate mechanical stresses on IRLA-PMSM rotor, each rotor layer can be considered as a rotating cylinder, whose material could present different properties along different directions (radial and tangential). Consequently, an advanced mechanical modelling of this specific geometric structure is introduced at first in order to determine both radial and tangential stresses on each cylinder [14]. This formulation can be then applied to the IRLA-PMSM rotor in order to assess layers retention at any speed and temperature within the given operating ranges, as detailed in the following.

A. Mechanical stresses on rotating cylinders

Referring to the schematic representation of a generic rotating cylinder shown in Fig. 2, it is assumed that the shear stresses can be neglected, thus the internal stress is due to radial and tangential strains only. Considering the generic infinitesimal portion of the cylinder, the Hooke's Law associates the radial displacement (u_r) to the deforming force as

$$\varepsilon_r = \frac{du_r}{dr} = \frac{1}{E_\theta}\left(k^2\sigma_r - \upsilon_\theta\sigma_\theta + E_\theta\alpha_r\Delta T\right) \tag{1}$$

$$\varepsilon_\theta = \frac{u_r}{r} = \frac{1}{E_\theta}\left(\sigma_\theta - k^2\upsilon_r\sigma_r + E_\theta\alpha_\theta\Delta T\right) \tag{2}$$

where ε_r and ε_θ are radial and tangential strains due to u_r, while σ_r and σ_θ denote the radial and tangential stresses. Furthermore, $E_{r,\theta}$, $\upsilon_{r,\theta}$ and $\alpha_{r,\theta}$ are the Young's modulus, the Poisson's ratio and the thermal expansion coefficient along radial and tangential directions respectively. In particular, $\alpha_{r,\theta}$ may determine additional strains depending on the difference between actual and reference temperatures (ΔT), which is assumed linearly distributed within the cylinder. In particular, ΔT and k are expressed as

$$\Delta T\left(r\right) = t_0 + t_1 r\,, \quad k = \sqrt{E_\theta \big/ E_r}\,. \tag{3}$$

Referring to σ_r and σ_θ, they depend on each other through the equilibrium equation of the theory of elastic mechanics as

$$\sigma_r + r\frac{d\sigma_r}{dr} - \sigma_\theta + \rho\omega_m^2 r^2 = 0 \tag{4}$$

where r is the radius of the infinitesimal portion of the cylinder, ρ is its mass density, and ω_m is the rotational speed. Consequently, properly combining (1)-(2) with (4) yields

$$\begin{aligned} r^2\frac{d^2\sigma_r}{dr^2} + 3r\frac{d\sigma_r}{dr} + \left(1-k^2\right)\sigma_r + \left(3+\upsilon_\theta\right)\rho\omega^2 r^2 + \\ + E_\theta\left(r\alpha_\theta\frac{d\Delta T}{dr} - \Delta T\left(\alpha_r + \alpha_\theta\right)\right) = 0\,. \end{aligned} \tag{5}$$

Solving (5) by imposing appropriate boundary conditions, the distribution of the radial stress in the cylinder is obtained as

$$\begin{aligned} \sigma_r\left(r\right) = c_1 r^{k-1} + c_2 r^{-k-1} - \frac{\left(3+\upsilon_\theta\right)\rho\omega^2 r^2}{9-k^2} + \\ - E_\theta\left(\frac{r\left(2\alpha_\theta - \alpha_r\right)t_1}{4-k^2} + \frac{\left(\alpha_\theta - \alpha_r\right)t_0}{1-k^2}\right). \end{aligned} \tag{6}$$

Differentiating (6) and substituting the resulting expression in (4), the distribution of tangential stress is achieved as

$$\begin{aligned} \sigma_\theta\left(r\right) = kc_1 r^{k-1} - kc_2 r^{-k-1} - \rho\omega^2 r^2\left(\frac{3\left(3+\upsilon_\theta\right)}{9-k^2} - 1\right) + \\ - E_\theta\left(\frac{2r\left(2\alpha_\theta - \alpha_r\right)t_1}{4-k^2} + \frac{\left(\alpha_\theta - \alpha_r\right)t_0}{1-k^2}\right) \end{aligned} \tag{7}$$

Still referring to (7), c_1 and c_2 can be obtained by imposing appropriate boundary conditions on the pressure acting on the internal and external surface of the cylinder ($p_{i/o}$), as detailed in (8) and (9) respectively, where r_o and r_i represent the outer and inner radii of the cylinder, as shown in both Fig. 2 and Fig. 3.

In conclusion, if isotropic materials are concerned, the following simplifications occur:

$$k = 1\,, \quad \upsilon_r = \upsilon_\theta = \upsilon\,, \quad E_r = E_\theta = E\,, \quad \alpha_r = \alpha_\theta = \alpha\,. \tag{10}$$

$$c_1 = \frac{p_i\dfrac{r_o^{-k-1}}{r_i^{-k-1}} - p_o - \dfrac{\left(3+\upsilon_\theta\right)\rho\omega^2}{9-k^2}\left(r_o^{\,2} - \dfrac{r_i^{3+k}}{r_o^{\,k+1}}\right)}{\left(r_i^{2k}r_o^{-k-1} - r_o^{\,k-1}\right)} - \frac{E_\theta\left(\dfrac{t_1\left(2\alpha_\theta - \alpha_r\right)}{4-k^2}\left(r_o - \dfrac{r_i^{k+2}}{r_o^{\,k+1}}\right) + \dfrac{t_0\left(\alpha_\theta - \alpha_r\right)}{1-k^2}\left(1 - \dfrac{r_o^{-k-1}}{r_i^{-k-1}}\right)\right)}{\left(r_i^{2k}r_o^{-k-1} - r_o^{\,k-1}\right)} \tag{8}$$

$$c_2 = \frac{p_i\dfrac{r_o^{\,k-1}}{r_i^{k-1}} - p_o - \dfrac{\left(3+\upsilon_\theta\right)\rho\omega^2}{9-k^2}\left(r_o^{\,2} - r_o^{\,k-1}r_i^{3-k}\right)}{\left(r_o^{\,k-1}r_i^{-2k} - r_o^{-k-1}\right)} - \frac{E_\theta\left(\dfrac{t_1\left(2\alpha_\theta - \alpha_r\right)}{4-k^2}\left(r_o - r_i^{2-k}\right) + \dfrac{t_0\left(\alpha_\theta - \alpha_r\right)}{1-k^2}\left(1 - \dfrac{r_o^{\,k-1}}{r_i^{k-1}}\right)\right)}{\left(r_o^{\,k-1}r_i^{-2k} - r_o^{-k-1}\right)} \tag{9}$$

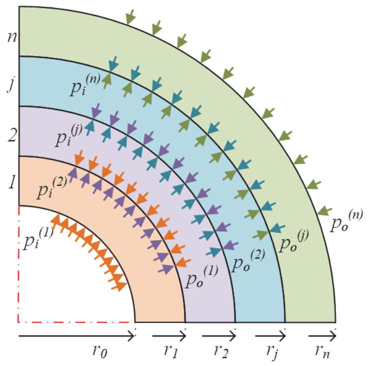

Fig. 3. Contact pressures map for n concentric cylinders.

Consequently, (6) and (7) become

$$\sigma_{r,isot}\left(r\right)=c_1+\frac{c_2}{r^2}-\frac{3+\upsilon}{8}\rho\omega^2r^2-\frac{t_1E\alpha}{3}r \tag{11}$$

$$\sigma_{\theta,isot}\left(r\right)=c_1-\frac{c_2}{r^2}-\frac{1+\upsilon}{8}\rho\omega^2r^2-2\frac{t_1E\alpha}{3}r\ . \tag{12}$$

B. Contact pressures between concentric cylinders

When two or more cylinders are concentrically mounted on each other and press-fitted together in order to ensure the adhesion of the cylinders at any condition, as occurs in IRLA-PMSM rotor, $p_{i/o}$ appearing in (8) and (9) represent the contact pressures between the cylinder surfaces, as highlighted in Fig. 3. The expression of $p_{i/o}$ can be achieved from u_r defined by (2) as

$$u_r^{(j)}=\frac{r}{E_\theta^{(j)}}\left(\sigma_\theta^{(j)}-k\upsilon_r^{(j)}\sigma_r^{(j)}+E_\theta^{(j)}\alpha_\theta^{(j)}\Delta T^{(j)}\right),\ \ j\in\left\{1..n\right\} \tag{13}$$

in which n is the number of cylinders. In addition, the radial interferences between two generic adjoining cylinders (δ), i.e. the difference between the outer radius of a cylinder and the free inner radius of the following adjoining cylinder, is

$$\left.\left(u_r^{(j)}-u_r^{(j-1)}\right)\right|_{r=r_j}=\delta_j\ ,\quad j\in\left\{2..n\right\}. \tag{14}$$

Consequently, based on (6)-(7) and (13)-(14), the pressure distribution on each cylinder can be achieved by imposing the following boundary conditions:

$$p_i^{(1)}=p_o^{(n)}=0\,,\quad p_o^{(j-1)}=-p_i^{(j)}\ ,\quad j\in\left\{2..n\right\}\ . \tag{15}$$

IV. IRLA-PMSM DESIGN

The design of IRLA-PMSM, whose main geometric variables are summarized in Table I, has been achieved through a multi-parameter analytical procedure, whose flowchart is depicted in Fig. 4. The procedure starts from a number of tuneable variables, which can vary within appropriate ranges. These variables, jointly with design targets and material properties, concur to determine derived variables through appropriate modelling relationships. As a result, a number of IRLA-PMSM configurations are achieved, each of which is represented by a multi-dimensional variable array. These configurations are further processed in order to disregard those that do not comply with mechanical, electromagnetic and energy constraints, which are detailed in the following subsections. Among all the remaining IRLA-PMSM configurations, the final geometry is selected by means of an optimization criterion, which is, in this case, the minimization of the active volume.

TABLE I. IRLA-PMSM GEOMETRIC VARIABLES

Variable	**Symbol**
Shaft radius	r_{sh}
Outer PM radius	r_m
Rotor yoke thickness	s_{yr}
PM thickness	s_m
Sleeve thickness	s_s
Stator outer radius	r_{st}
Stator yoke	s_{ys}
Slot height	h_s
Active length	l_i

A. Mechanical constraints

In order to guarantee rotor layer retention and to avoid mechanical failure, it is necessary to impose that internal and external contact pressures ($p_{i/o}$) acting on each rotor layer (y), namely rotor yoke (yr), PM ring (m) and sleeve (s), are always greater than zero, as well as that all mechanical stresses are within their corresponding allowable ranges.

Assuming isotropic materials at first, the following relationships should be satisfied:

$$\begin{gathered}p_{i/o}^{(y)}>0\,,\quad\left|\sigma_{VM}^{(y)}\right|<\left|\frac{\sigma_{VM,max}^{(y)}}{s_f}\right|,\quad y\in\left\{yr,m,s\right\}\\ \sigma_{VM}=\sqrt{{\sigma_{r,isot}}^2+{\sigma_{\theta,isot}}^2-\sigma_{r,isot}\sigma_{\theta,isot}}\end{gathered} \tag{16}$$

in which s_f is a safety coefficient, while σ_{VM} is the Von Mises' stress, which depends on both radial and tangential stresses defined in (11)-(12).

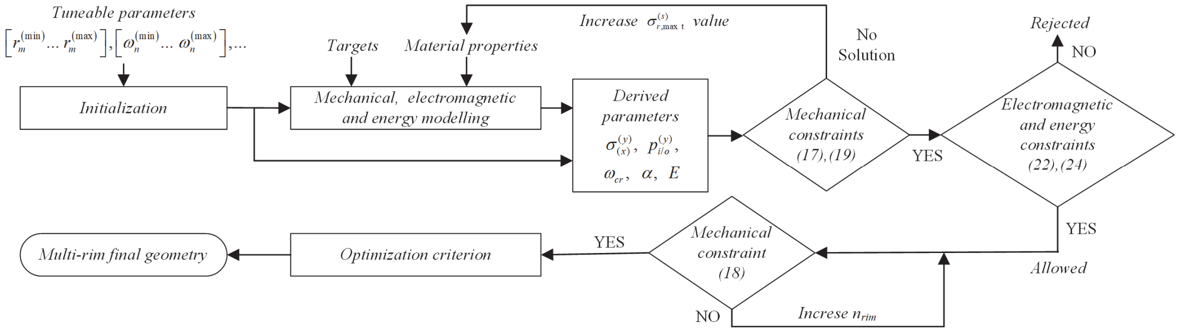

Fig. 4. Flowchart of the design procedure used for IRLA-PMSM.

TABLE II. FESS MATERIAL PROPERTIES

Description	**Symbol**	**Unit**	**Value**
Flywheel/Sleeve (CFRP 60%)			
Specific mass density	$\rho^{(s)}$	kg/m^3	1500
Radial Young's modulus	$E^{(s)}{}_r$	MPa	10000
Tangential Young's modulus	$E^{(s)}{}_\theta$	MPa	150000
Radial Poisson's ratio	$\upsilon^{(s)}{}_r$	-	0.02
Tangential Poisson's ratio	$\upsilon^{(s)}{}_\theta$	-	0.34
Tensile radial max stress	$\sigma^{(s)}{}_{r,max\_t}$	MPa	10
Compression radial max stress	$\sigma^{(s)}{}_{r,max\_c}$	MPa	200
Tensile tangential max stress	$\sigma^{(s)}{}_{\theta,max\_t}$	MPa	2800
Compression tangential max stress	$\sigma^{(s)}{}_{\theta,max\_c}$	MPa	1500
Rotor and Stator Cores (Silicon Steel)			
Specific mass density	$\rho^{(yr)}$	kg/m^3	7600
Young's modulus	$E^{(yr)}$	MPa	185000
Poisson's ratio	$\upsilon^{(yr)}$	-	0.30
Max stress	$\sigma^{(yr)}{}_{max}$	MPa	700
Permanent Magnets (Ferrite)			
Specific mass density	$\rho^{(m)}$	kg/m^3	5000
Young's modulus	$E^{(m)}$	MPa	180000
Poisson's ratio	$\upsilon^{(m)}$	-	0.28
Tensile max stress	$\sigma^{(m)}{}_{max\_t}$	MPa	60
Compression max stress	$\sigma^{(m)}{}_{max\_c}$	MPa	600
Magnetic remanence	$B_r{}^{(m)}$	T	0.4

In this regard, it is worth noting that the Von Mises' criterion is widely suggested in the literature for rotor mechanical stress evaluation, especially when sleeve design is concerned. However, it is suitable when all layer materials is isotropic and homogenous, such as steel or titanium [14]–[16], whereas it results inappropriate for IRLA-PMSM; this is because the sleeve consists of a thick cylinder of carbon fibre epoxy composite, which is an orthotropic material that presents very different mechanical properties along radial and tangential directions, as highlighted in Table II. Consequently, the use of (16) is inappropriate for designing the sleeve/flywheel of the proposed IRLA-PMSM, namely σ_r and σ_θ should be computed in accordance with (6) and (7), and they should be verified individually to guarantee the rotor retention, leading to

$$\left|\sigma_x^{(y)}\right| < \left|\frac{\sigma_{x,max}^{(y)}}{s_f}\right|, \quad x \in \{r,\theta\}, \quad y \in \{yr,m,s\}. \tag{17}$$

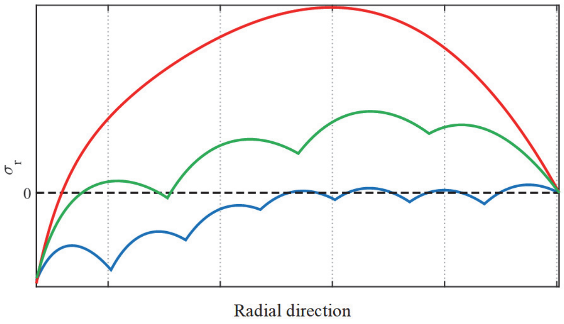

Fig. 5. Typical radial stress evolution achieved on the sleeve by using different number of rims: 1 rim (red line); 4 rims (green line); 7 rims (blue line).

However, apart from (17), the low mechanical tensile strength of the epoxy-matrix in radial direction limits the maximum thickness of the sleeve. Consequently, since a large sleeve thickness is foreseen in order to store the required amount of energy (8 kWh), reference should be made to a multi-rim structure, which involves more cylindrical elements (rims) coupled to each other with interference [12], [13]; this structure limits the maximum stress along the radial direction, thus enabling adequate sleeve thickness, as well shown in Fig. 5. Therefore, the proposed design procedure accounts for the multi-rim structure of the sleeve, but not directly because this would increase the already very large number of tunable variables involved; as a result, the design procedure would be less effective and much more complicated than that employed for isotropic materials. Consequently, an equivalent single-rim structure has been considered, whose maximum tensile stress $\sigma^{(s)}{}_{r,max\,t}$ has been gradually increased until complying with (17). Subsequently, the equivalent single-rim structure is split into an increasing number of rims, whose radial stress distribution must comply with the maximum stress values reported in Table II. Consequently, (17) is joined by the following relationship:

$$\left|\sigma_x^{(y)}\right| < \left|\frac{\sigma_{x,max}^{(y)}}{s_f}\right|, \quad x \in \{r,\theta\}, \quad y \in \left\{s_1 .. s_{n_{rim}}\right\} \tag{18}$$

where n_{rim} is the number of the employed rims, namely the minimum number of rims that enables satisfying (18).

Apart from stress constraints, also the mechanical resonance phenomena should be considered. Consequently, the critical rotor speed should be evaluated and it should be set reasonably higher than IRLA-PMSM maximum speed as

$$\omega_{m,\max} \ll \omega_{cr}\,, \quad \omega_{cr} = \sqrt{\psi / M} \tag{19}$$

in which ψ is stiffness of the shaft to transverse vibrations and M is the rotor mass. It is worth noting that (19) allows just a roughly estimation of the rotor critical speed, thus detailed analyses should be made by finite element methods to avoid any failure within the system operating boundaries.

B. Electromagnetic constraints

From an electromagnetic point of view, PM demagnetization has to be prevented at any operating condition, by enabling an adequate flux-weakening capability at the same time. Therefore, referring to the magnetic flux densities due to stator *mmf* ($\tilde{B}_m$) and to PMs ($\bar{B}_m$) separately, the following relationship should be imposed [9]:

$$\tilde{B}_m = \alpha \bar{B}_m \tag{20}$$

in which α denotes the magnetic ratio, which should be within (0,1). Regarding $\tilde{B}_m$ and $\bar{B}_m$, their general expressions can be achieved under some assumptions by applying both Ampere's and Gauss' laws [9], leading to:

$$\tilde{B}_m \propto n \cdot I_{eq}\,, \quad \bar{B}_m \propto -2 s_m H_c \tag{21}$$

where n and I_{eq} are the equivalent turns and current of the machine winding, whose product represents the overall stator *mmf*, while H_c is the PM coercive force. Consequently, by substituting (21) into (20), the following inequality is achieved:

$$-\frac{n \cdot I_{eq}}{2 s_m H_c} \le \alpha^* \tag{22}$$

TABLE III. IRLA-PMSM MAIN PARAMETERS AND RATED VALUES

Description	Symbol	Unit	Value
Rated power	P_n	kW	8
Storable/deliverable energy	E	kWh	8
Rated speed	$\omega_{m,n}$	rpm	10000
Maximum speed	$\omega_{m,max}$	rpm	30000
Rated torque	T_e	Nm	7.64
Rated current	I_n	A	62
Rated voltage	E_n	V	84
Pole pairs	p	[-]	1
Magnetic ratio	α	[-]	0.67
Radial interference	δ	mm	0.1-0.9
Shaft radius	r_{sh}	mm	29
Rotor yoke thickness	s_{yr}	mm	29
PM thickness	s_m	mm	10
Sleeve thickness	s_s	mm	233
Rim thickness	s_{rim}	mm	33.2
Rim number	n_{rim}	-	7
Air-gap	s_g	mm	1
Stator outer radius	r_{ys}	mm	333
Stator yoke	s_{ys}	mm	18
Slot height	h_s	mm	13.5
Active length	l_i	mm	340
Rotor/flywheel mass	M	kg	171
Safety factor	s_f	-	2

where α^* is the maximum allowable value of α in order to prevent PM demagnetization properly [9].

C. *Energy constraints*

The energy constraint can be set as:

$$E_{rotor}\big|_{\omega_{m,max}} - E_{rotor}\big|_{\omega_{m,n}} \ge E^* \ , \quad E_{rotor} = \frac{1}{2} J \omega_m^{\ 2} \tag{23}$$

in which E_{rotor} denotes the energy stored by the IRLA-PMSM rotor at a given speed, J represents the inertia coefficient of the rotor mass, and E^* is the amount of energy that should be exchanged by FESS over its full operating range (8 kWh). As a result, combining (23) to each other yields:

$$\omega_{m,\max}^2 - \omega_{m,n}^2 \ge \frac{2E^*}{J} \ . \tag{24}$$

In conclusion, it is worth noting that the minimum operating speed of FESS is the IRLA-PMSM rated speed in order to always exchange energy at constant-power operation.

V. ANALYTICAL AND FINITE ELEMENT ANALYSIS RESULTS

The main design parameters of the final geometry of the proposed IRLA-PMSM are summarized in Table III, together with its rated values. Regarding the sleeve/flywheel, 7 rims have been chosen, which are characterized by increasing interferences (from 0.1 mm to 0.9 mm) in order to satisfy all the mechanical constraints. In particular, the most critical aspect is represented by σ_r acting on the sleeve at maximum speed (30 krpm) due to the very low σ_r allowable by the epoxy-matrix (Table II).

Regarding PMs, they have been preliminary assumed as a continuous ring, without accounting for PM segmentation and glue for the sake of simplicity. Similarly, thermal effects on stress distribution within IRLA-PMSM have been neglected at this stage; this simplification is because all these aspects will require accurate selection of PM shapes and filling materials, as well as losses assessment and spatial distribution, which will be considered in future investigations.

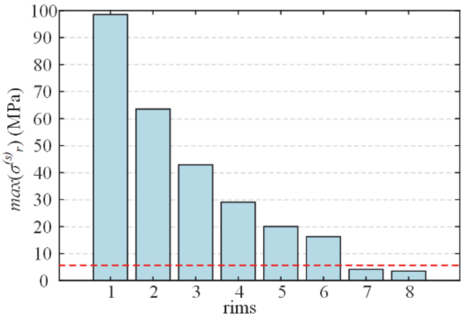

Fig. 6. Maximum $\sigma^{(s)}_r$ achieved on the sleeve by using different number of rims, together with the maximum $\sigma^{(s)}_r$ of the material (red dotted line, which already accounts for the safety factor s_f).

A. *Mechanical analytical results*

Fig. 6 highlights the maximum radial stress acting on the sleeve for the proposed configuration, which is achieved through analytical computation by considering different number of rims. In each case, optimal interference values have been considered in order to reduce the radial stress, by complying with all the other constraints at any operating condition. From Fig. 6 it is clear that seven is the minimum number of rims required by the proposed IRLA-PMSM in order to avoid mechanical failure at any operating condition.

The distribution of σ_r and σ_θ in the rotor along the radial direction at zero and maximum speed (30 krpm), which have been achieved by analytical computation, are shown in Fig. 7 and Fig. 8 respectively. In particular, Fig. 7 shows that the radial interference values guarantee allowable prestresses in each layer, which are within the compression stress limit of the composite material in radial direction ($\sigma^{(s)}_{r\_max\ c}$). Consequently, these prestresses and the use of a multi-rim structure make the maximum tensile stress in the radial direction at maximum speed within the limits of the materials (Fig. 8), even by considering an adequate safety factor ($s_f = 2$). It is worth noting that these figures show some discontinuities in stress evolutions, which correspond to the contact surfaces between the different rims; these are due to the appropriate radial interference values that reduce the maximum value of σ_r within the limits of the material, as pointed out previously.

B. *Mechanical FEA results*

The distributions of σ_θ and σ_r in the sleeve at $\omega_{m,max}$ achieved by FEA are shown in Fig. 9 and Fig. 10. It can be seen that σ_θ is higher on the inner surface of the outer rim, while it decreases moving from outer to inner layers, as expected. The maximum value achieved for tangential stress is about 1400 MPa, which well matches that obtained analytically (Fig. 8). In addition, this value is much lower than the maximum stress allowable by the carbon-fibre material (approximately 2800 MPa), even considering $s_f = 2$. Similar considerations apply to σ_r at $\omega_{m,max}$ (Fig. 10), which reveals very low stress values that increase along the radial direction, and that well match those achieved analytically (Fig. 8).

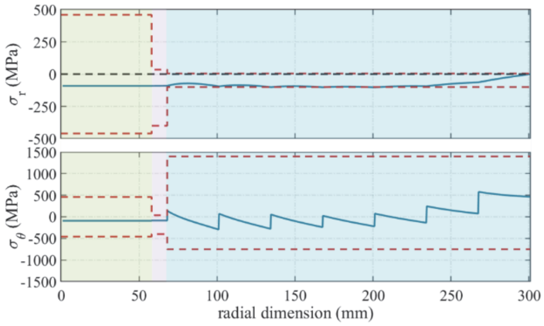

Fig. 7. Radial (top) and tangential (bottom) stress evolutions at zero speed, together with their corresponding boundaries (red-dot lines, which already accounts for s_f): shaft + rotor yoke (green zone), PMs (purple zone), and flywheel/sleeve (blue zone).

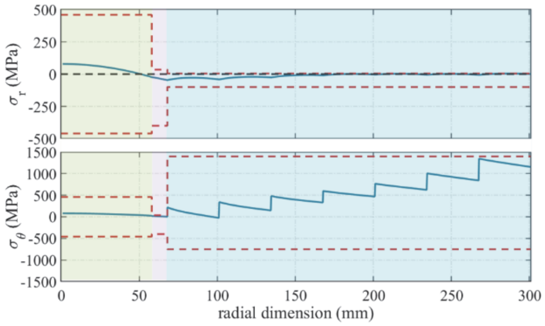

Fig. 8. Radial (top) and tangential (bottom) stress evolutions at maximum speed, together with their corresponding boundaries (red-dot lines, which accounts for s_f): shaft + rotor yoke (green zone), PMs (purple zone), and flywheel/sleeve (blue zone).

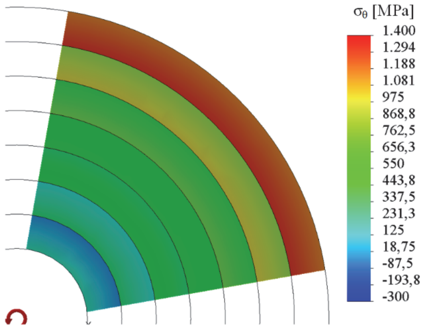

Fig. 9. Sleeve tangential stress distribution at maximum speed.

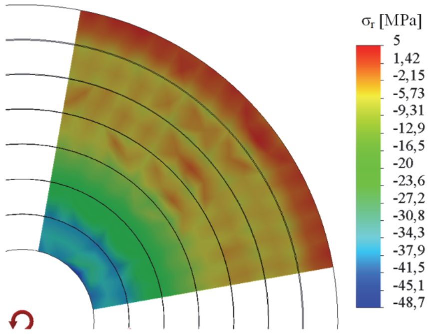

Fig. 10. Sleeve radial stress distribution at maximum speed.

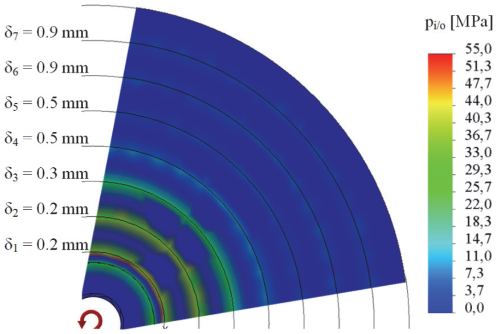

Fig. 11. Rotor contact pressures distribution at maximum speed, together with rim radial interferences.

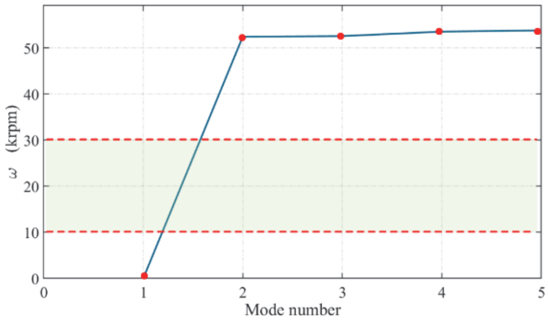

Fig. 12. Different rotor critical speeds (red dots), togheter with rotor operating speed range (green zone bounded by red dotted lines).

The contact pressures distribution at the maximum speed (the worst operating condition) is shown in Fig. 11, which reveals that $p_i^{(m)}$ is about 20 MPa and that the contact pressures between each pair of rims are greater than zero. Consequently, torque transmission and PM retention are both ensured properly. On the other hand, Fig. 12 highlights different critical rotor speed values corresponding to different undamped natural frequencies of the rotor computed through 3D FEA. It can be seen that IRLA-PMSM operates in a safety range between the first and the second critical speed of the rotor. It is clear that, when the machine is started, the rotor speed could match the first critical speed, which presents a very low value, before reaching the minimum operating speed (10 krpm). However, this critical value is assumed passed as quickly as possible to avoid any external mechanical perturbation or interference.

C. Electromagnetic FEA results

The electromagnetic FEA results are reported from Fig. 13 to Fig. 15. The magnetic flux density distribution at rated speed (Fig. 13) reveals quite low values compared to magnetic saturation thresholds of the iron core material (approximately 1.3 T); this is expected due to the large equivalent airgap of the proposed IRLA-PMSM, which results in a weak magnetic exploitation of the iron core material. However, this is an important advantage for minimizing iron losses and back-emf magnitudes, enabling high-speed operation. Furthermore, the phase back-emf evolutions achieved at rated speed (Fig. 14) highlight good sinusoidal shapes, quite similar to the ideal ones, and their magnitudes fairly match those obtained by the analytical procedure (Table III). Regarding the electromagnetic torque, Fig. 15 shows the 2D FEA results achieved at rated load and speed by employing the maximum-torque-per-ampere control strategy; the torque and its ripple are approximately 7.8 Nm and 3%, revealing the effectiveness of the proposed design.

VI. CONCLUSION

The design of Inner-Rotor Large-Airgap Surface-Mounted

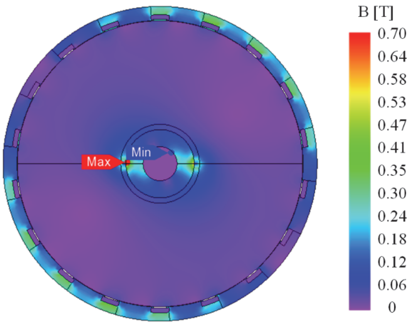

Fig. 13. Magnetic flux density distribution at ω_m = 10 krpm and T_e = 7.6 Nm.

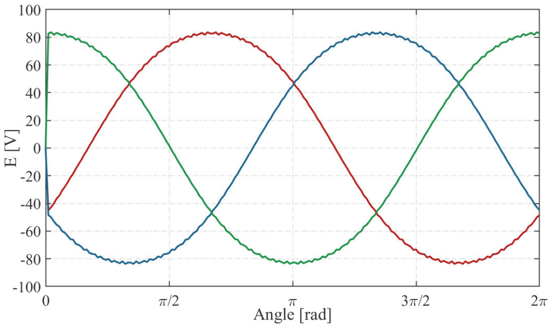

Fig. 14. Back-emf evolutions at rated speed.

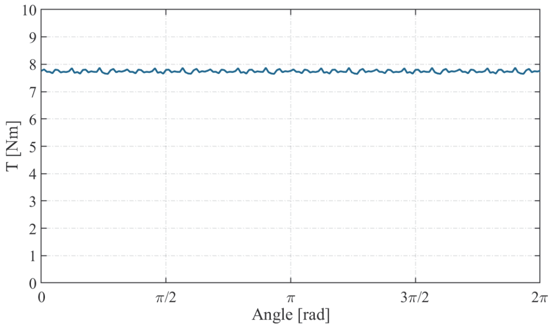

Fig. 15. Torque evolutions at rated load and speed.

Permanent Magnet Synchronous Machine (IRLA-PMSM) that integrates a carbon-fibre flywheel has been presented in this paper. The design has been achieved by an advanced mechanical modelling integrated within a multi-parameter analytic design procedure that accounts also for electromagnetic and energy aspects. The effectiveness of the preliminary analytical design has been validated by finite element analyses, which have regarded both mechanical and electromagnetic aspects. The results show the effectiveness of the proposed design approach, especially in complying with strict mechanical constraints introduced by orthotropic materials with multi-rim structures. However, further investigations and refinements are needed, among which an extensive performance assessment, losses evaluation and, consequently, a thermal analysis. The last step is the prototyping stage for experimental validation. All these aspects will be considered in future works.

Acknowledgment

This work has been developed within the project KINITIKI, which has been funded by the Sardinian Regional Government through Sardegna Ricerche under the Grant Agreement no. 1C-170 (Aids to R&D projects, POR FESR 2014-2020, Action 1.1.3).

References

[1] A. A. K. Arani, H. Karami, G. B. Gharehpetian, and M. S. A. Hejazi, ‘Review of Flywheel Energy Storage Systems structures and applications in power systems and microgrids’, *Renewable and Sustainable Energy Reviews*, vol. 69, pp. 9–18, Mar. 2017.

[2] R. Sebastián and R. Peña Alzola, ‘Flywheel energy storage systems: Review and simulation for an isolated wind power system’, *Renewable and Sustainable Energy Reviews*, vol. 16, no. 9, pp. 6803–6813, Dec. 2012.

[3] S. M. Mousavi G, F. Faraji, A. Majazi, and K. Al-Haddad, ‘A comprehensive review of Flywheel Energy Storage System technology’, *Renewable and Sustainable Energy Reviews*, vol. 67, pp. 477–490, Jan. 2017.

[4] P. Yulong, A. Cavagnino, S. Vaschetto, C. Feng, and A. Tenconi, ‘Flywheel energy storage systems for power systems application’, in *Proc. of 6th International Conference on Clean Electrical Power (ICCEP 2017)*, Jun. 2017, pp. 492–501.

[5] N. Bernard, H. B. Ahmed, B. Multon, C. Kerzreho, J. Delamare, and F. Faure, ‘Flywheel energy storage systems in hybrid and distributed electricity generation’, p. 9, 2003.

[6] X. Li, N. Erd, and A. Binder, ‘Design and calculation of a 130 kW high-speed permanent magnet synchronous machine in flywheel energy storage systems for urban railway application’, in *Proc. of 6th International Conference on Clean Electrical Power (ICCEP 2017)*, Jun. 2017, pp. 452–459.

[7] H. Thomaschewski, T. Turnbull, J. Sandercock, T. Matthews, J. P. Prévost, and S. Deleanu, ‘Illustration of flywheel energy storage system performance for engineering technology students’, in *Proc. of International Conference on Modern Power Systems (MPS 2017)*, Jun. 2017, pp. 1–8.

[8] G. Fois, A. Floris, A. Serpi, M. Porru, and A. Damiano, ‘Design Criteria for Ferrite-Based High-Speed Permanent Magnet Synchronous Machines’, presented at the 7th International Electric Drives Production Conference (EDPC 2017), Wuerzburg (Germany), Dec. 2017.

[9] A. Damiano, A. Floris, G. Fois, I. Marongiu, M. Porru, and A. Serpi, ‘Design of a High-Speed Ferrite-Based Brushless DC Machine for Electric Vehicles’, *IEEE Transactions on Industry Applications*, vol. 53, no. 5, pp. 4279–4287, Sep. 2017.

[10] A. Floris, A. Serpi, M. Porru, G. Fois, and A. Damiano, ‘Design of a Double-Stage Magnetic Gear for High-Speed Electric Propulsion Systems’, in *Proc. of XIII International Conference on Electrical Machines (ICEM’2018)*, Sep. 2018, pp. 670–676.

[11] J. Brunbauer and G. Pinter, ‘Effects of mean stress and fibre volume content on the fatigue-induced damage mechanisms in CFRP’, *International Journal of Fatigue*, vol. 75, pp. 28–38, Jun. 2015.

[12] S. J. Kim, K. Hayat, S. U. Nasir, and S. K. Ha, ‘Design and fabrication of hybrid composite hubs for a multi-rim flywheel energy storage system’, *Composite Structures*, vol. 107, pp. 19–29, Jan. 2014.

[13] S. Ha, H. Han, and Y. Han, ‘Design and Manufacture of a Composite Flywheel Press-Fit Multi-Rim Rotor’, *Journal of Reinforced Plastics and Composites - J REINF PLAST COMPOSITE*, vol. 27, pp. 953–965, Jan. 2008.

[14] L. Chen and C. Zhu, ‘Strength Analysis for Surface-mounted Permanent Magnet Rotor in High-Speed Motor’, *TELKOMNIKA Indonesian Journal of Electrical Engineering*, vol. 12, no. 10, pp. 7131–7142, Oct. 2014.

[15] P. D. Pfister and Y. Perriard, ‘A 200 000 rpm, 2 kW slotless permanent magnet motor’, in *Proc. of 11th International Conference on Electrical Machines and Systems (ICEMS 2008)*, Wuhan (China), Oct. 2008, pp. 3054–3059.

[16] Z. Huang and J. Fang, ‘Multiphysics Design and Optimization of High-Speed Permanent-Magnet Electrical Machines for Air Blower Applications’, *IEEE Transactions on Industrial Electronics*, vol. 63, no. 5, pp. 2766–2774, May 2016.